

Thermal conductivities of monolayer graphene oxide from machine learning molecular dynamics simulations

Bohan Zhang,^{1,*} Biyuan Liu,^{2,*} Penghua Ying,^{3,4,†} Zherui Chen,^{5,6} Yanzhou Wang,^{7,8} Yonglin Zhang,² Haikuan Dong,¹ Jinglei Yang,^{2,9,‡} and Zheyong Fan^{1,§}

¹College of Physical Science and Technology, Bohai University, Jinzhou 121013, P. R. China

²Department of Mechanical and Aerospace Engineering,

Hong Kong University of Science and Technology, Clear Water Bay, Kowloon, Hong Kong

³Department of Physical Chemistry, School of Chemistry, Tel Aviv University, Tel Aviv, 6997801, Israel

⁴Laboratory for multiscale mechanics and medical science, SV LAB,
School of Aerospace, Xi'an Jiaotong University, Xi'an 710049, China

⁵Future Technology School, Shenzhen Technology University, Shenzhen 518118, P. R. China

⁶College of Applied Sciences, Shenzhen University, Shenzhen 518060, P. R. China

⁷School of Electronic Engineering, Chengdu Technological University, Chengdu 611730, China

⁸Department of Applied Physics, Aalto University, FIN-00076 Aalto, Espoo, Finland

⁹HKUST Shenzhen-Hong Kong Collaborative Innovation Research Institute, Futian, Shenzhen, China

(Dated: December 29, 2025)

Graphene oxide (GO) exhibits rich chemical heterogeneity that strongly influences its structural, thermal, and mechanical properties, yet quantitatively linking reduction chemistry to heat transport remains challenging. In this work, we develop a machine-learned neuroevolution potential (NEP) trained on an existing density functional theory dataset (*Angew. Chem. Int. Ed.*, **63**, e202410088 (2024)), achieving reasonable accuracy at a computational cost much lower than the existing machine-learned and empirical potentials. Leveraging this potential, we perform large-scale molecular dynamics (MD) simulations to model the thermal reduction of GO across realistic structural domains. Using the homogeneous nonequilibrium MD method with a proper quantum-statistical correction scheme, we find that reduced GO exhibits strongly suppressed thermal conductivities, ranging from a few to tens of $\text{Wm}^{-1}\text{K}^{-1}$, substantially lower than pristine GO without defects and far below graphene. Moreover, the thermal conductivity of reduced GO increases moderately with increasing OH/O ratio, except at the highest oxidation level (O/C=0.5) where this trend inverts, while decreasing significantly with increasing O/C ratio, a trend strongly correlated with the fraction of recovered graphene-like structures. Our work provides a computationally tractable and predictive atomistic machine learning framework for exploring how chemical structure governs heat transport in heterogeneous carbon materials.

I. INTRODUCTION

The physicochemical properties of graphene oxide (GO) are determined by the interactions between graphene and various oxygen functional groups, including epoxides, hydroxyls, and carbonyls [1]. These distinct chemical features give rise to unique mechanical, thermal, and transport characteristics, rendering GO a critical material for thermal management, membrane separation, and energy storage [2]. Despite its practical importance, a quantitative understanding of how chemical reduction influences heat transport in GO remains inadequate. Structural complexities, such as diverse functional groups, local bonding configurations, and defect topologies, introduce strong phonon-scattering pathways, making the heat transfer mechanisms difficult to accurately quantify [3]. Consequently, establishing the fundamental relationship between reduction chemistry and thermal

conductivity in GO remains a prominent and unresolved challenge in the field.

Over the past decade, experimental research has demonstrated that the thermal conductivities of GO and reduced graphene oxide (rGO) depend heavily on the degree of oxidation and reduction [4]. Early experiments on GO films reported in-plane thermal conductivities of only a few $\text{Wm}^{-1}\text{K}^{-1}$, confirming the strong phonon-scattering effect of oxygen functional groups [5]. Due to complex microstructural reconstruction during reduction [4], experimentally pinpointing the precise influence of the oxygen-to-carbon (O/C) and the hydroxyl-to-epoxide (OH/O) ratios remains difficult. The stochastic nature of reduction introduces significant structural uncertainty, making it impossible to experimentally control these ratios independently. Consequently, theoretical predictions are required to disentangle these chemical variables and accurately quantify their individual impacts on thermal transport.

Classical molecular dynamics (MD) provides a powerful framework for probing phonon scattering, defect interactions, and heat transport in structurally disordered materials such as GO at experimentally relevant length scales. However, the predictive accuracy of MD is fundamentally limited by the fidelity of the underlying in-

* These authors contributed equally to this work.

† hityingph@tauex.tau.ac.il

‡ maeyang@ust.hk

§ brucenju@gmail.com

teratomic potential. Widely used empirical force fields, such as reactive force-field (ReaxFF) [6], often fail to capture the diverse and evolving carbon-oxygen bonding environments inherent to GO reduction. This limitation may lead to inconsistent thermal conductivity predictions and inaccurate descriptions of oxygen functional-group energetics [7, 8]. Consequently, these deficiencies introduce substantial uncertainty in modeling chemistry-transport relationships, underscoring the critical need for interatomic potentials that balance high accuracy with the computational efficiency required for reactive C/H/O systems.

Machine-learned potentials (MLPs) have recently emerged as a powerful alternative to empirical force fields to drive MD simulations, offering near-density functional theory (DFT) accuracy with far lower cost [9, 10]. Notably, the MACE architecture [11] has been successfully applied to investigate the thermal reduction mechanisms [12] and mechanical properties [12] of GO. However, despite these successes, the MACE architecture remains computationally intensive, making it unsuitable for thermal conductivity calculations that require extensive molecular dynamics sampling [13]. To accurately model the O/C- and OH/O-ratio-dependent thermal transport in rGO, which demands long simulation trajectories, a reactive yet highly scalable interatomic potential is essential.

Here, we introduce NEP-GO, a specialized neuroevolution potential (NEP) model developed for GO. Our model is built upon the state-of-the-art NEP framework [14–16], which has been widely adopted in modeling complex materials [13, 17]. By leveraging this efficient architecture, NEP-GO achieves computational speeds and system sizes several orders of magnitude faster than MACE, given a consistent reference dataset. This performance breakthrough allows for the construction of a transferable and efficient model for GO, facilitating the large-scale atomistic simulations essential for capturing thermal reduction processes and their impact on thermal conductivity.

II. METHODS

A. NEP training

We constructed a MLP for GO and rGO employing the NEP framework implemented in the GPUMD package (version 4.3) [18]. The NEP approach, specifically designed for efficient MD simulations, adopts the atomic environment descriptor methodology established by Behler and Parrinello [9]. In this scheme, the site energy of an atom is modeled via an artificial neural network (ANN) using a high-dimensional descriptor vector invariant to translation, rotation, and permutation of atoms of the same species. The trainable parameters in the model are optimized using the separable natural evolution strategy (SNES) [19].

Training data were sourced from the DFT dataset generated by El-Machachi *et al.* [12], comprising 3,816 structures. We only excluded three isolated-atom configurations that are not needed for the NEP method. The NEP model architecture was established with a radial cutoff of 4.2 Å and an angular cutoff of 3.7 Å. These relatively short cutoffs were partially motivated by the choice in the previous MACE model [12], which used a cutoff of 3.7 Å. The descriptors employ nine radial functions and seven angular radial functions, each expressed as a linear combination of nine basis functions. The angular components include three-body descriptors up to $l = 4$ and four-body descriptors up to $l = 2$ in the spherical harmonics expansion. The fitting neural network comprises a single hidden layer with 50 neurons. The model was trained for 200,000 steps using a full-batch training strategy. The loss function is a weighted sum of root mean square errors (RMSEs) of total energy, atomic forces, and virial tensors, as well as regularization terms.

B. Thermal reduction simulations

We employed the trained NEP model to perform large-scale MD simulations of the thermal reduction of GO to rGO. This process involves the transformation and eventual removal of oxygen-containing functional groups, accompanied by the release of gaseous byproducts such as H₂O, CO₂, and CO.

To generate the initial structures, we sampled the N -dimensional parameter space $\mathbf{P} = [p_1, \dots, p_N]$ defined in Ref. 12. The parameters determining the composition and arrangement of functional groups were selected as: (1) the oxygen-to-carbon ratio (O/C); (2) the hydroxyl fraction (OH/O), defined as the proportion of oxygen atoms belonging to hydroxyl groups; and (3) the ratio of functionalized edges to hydrogen-terminated edges.

For the simulations in this work, the fraction of functionalized edges was consistently set to zero (purely hydrogen-terminated edges). We generated two distinct series of GO structures. In the first series, the O/C ratio was fixed at 0.4 while the hydroxyl fraction (OH/O) was systematically varied from 0.1 to 0.5, corresponding to parameter vectors $\mathbf{P} = [0.4, 0.1 - 0.5, 0]$. In the second series, the OH/O ratio was held constant at 0.3 while the O/C ratio was varied from 0.1 to 0.5, corresponding to vectors $\mathbf{P} = [0.1 - 0.5, 0.3, 0]$. The resulting models contain 11033 to 17395 atoms. These structures capture key characteristics of GO, including topological disorder in the carbon backbone (e.g., non-hexagonal rings), while ensuring all carbon atoms remain threefold-coordinated without large pores or vacancies.

All MD simulations were performed using the GPUMD package (version 4.3) [18] with an integration time step of 0.1 fs. rGO structures were generated through a sequential equilibration, heating, annealing, and quenching protocol, with temperature control using the Langevin thermostat [20] with a damping parameter of 50 fs.

To determine the optimal reduction conditions, the thermal reduction process was initially evaluated at temperatures of 700 K, 800 K, 900 K, and 1200 K. We observed that annealing at 900 K yields structurally stable rGO, achieving an appropriate degree of reduction while preserving sufficient mechanical integrity. Consequently, 900 K was selected as the annealing temperature for all subsequent simulations. This is quantitatively different from Ref. [12], which employed a reduction temperature of 1500 K; we adopted 900 K specifically to avoid over-reduction and maintain a moderate residual oxygen content.

The rGO generation protocol proceeded as follows: First, each GO configuration was equilibrated at 300 K for 10 ps, and then rapidly heated to the target reduction temperature of 900 K over 0.1 ns, corresponding to a heating rate of 6 K ps⁻¹. Following this, the reduction and annealing stages were carried out at constant temperature for 1.9 ns. Finally, the system was quenched to 300 K within 0.1 ns and further equilibrated at this temperature for 0.1 ns. Throughout the entire process, detached fragments and gaseous byproducts were periodically removed to preserve the integrity of the graphene sheet. To account for the stochastic nature of the thermal reduction process, five independent simulations were performed for each specific parameter \mathbf{P} .

C. Thermal conductivity calculations

Thermal transport simulations were performed using the homogeneous nonequilibrium molecular dynamics (HNEMD) method [21] within the canonical (NVT) ensemble employing the Bussi-Donadio-Parrinello thermostat [22], as implemented in the GPUMD package (version 4.3) [18]. For each case, a production run of 3 ns was performed following 0.2 ns equilibration at 300 K.

In the HNEMD method, a steady-state heat current is induced by applying an external driving force $\mathbf{F}_i^{\text{ext}}$ to each atom i as follows [21, 23]:

$$\mathbf{F}_i^{\text{ext}} = \mathbf{F}_e \cdot \mathbf{W}_i, \quad (1)$$

where \mathbf{F}_e is the driving force parameter (with dimensions of inverse length) and was set to $1 \times 10^{-3} \text{ \AA}^{-1}$ in all simulations, and \mathbf{W}_i is the 3×3 atomic virial tensor of atom i defined as [14]

$$\mathbf{W}_i = \sum_{j \neq i} \mathbf{r}_{ij} \otimes \frac{\partial U_j}{\partial \mathbf{r}_{ji}}, \quad (2)$$

here $\mathbf{r}_{ij} \equiv \mathbf{r}_j - \mathbf{r}_i$, \mathbf{r}_i is the position of atom i , and U_j is the site energy of atom j .

Within the framework of linear-response theory, the non-equilibrium ensemble-averaged heat current \mathbf{J} is proportional to the driving-force parameter \mathbf{F}_e :

$$\langle J^\alpha \rangle = TV \sum_i \kappa^{\alpha\beta} F_e^\beta, \quad (3)$$

where T and V denote the system temperature and volume, respectively, and $\kappa^{\alpha\beta}$ is the thermal conductivity tensor. We compute the instantaneous heat current using the definition [24],

$$\mathbf{J} = \sum_i \mathbf{W}_i \cdot \mathbf{v}_i, \quad (4)$$

where \mathbf{v}_i denotes the velocity of atom i .

In the HNEMD approach, the frequency dependent spectral thermal conductivity $\kappa(\omega)$ is directly accessible through Fourier transformation of the velocity-virial autocorrelation function [21]

$$\mathbf{K}(t) = \sum_i \langle \mathbf{W}_i(0) \cdot \mathbf{v}_i(t) \rangle. \quad (5)$$

The summation runs over all atoms within the system. For simplicity, and because the in-plane thermal transport in graphene based materials is statistically isotropic, we consider only the diagonal components of the thermal conductivity tensor and henceforth drop the tensorial indices, denoting the scalar thermal conductivity simply as κ (and similarly $\kappa(\omega)$ for its spectral counterpart). The spectral thermal conductivity is obtained via Fourier transform of the virial-velocity autocorrelation function:

$$\kappa(\omega, T) = \frac{2}{VTF_e} \int_{-\infty}^{\infty} dt e^{i\omega t} K(t), \quad (6)$$

where the explicit temperature dependence of the spectral thermal conductivity has been highlighted.

III. RESULTS AND DISCUSSION

The NEP model developed in this work was trained on the dataset reported in Ref. [12]. For comparison, we also evaluated the MACE model trained based on the same reference data [12] and the ReaxFF model developed in Ref. [25].

As shown in Figure 1(a), the NEP model achieves good agreement with the DFT reference calculations for total energy, with an energy RMSE of 10.2 meV atom⁻¹. For atomic forces (Figure 1(b) and (c)), both NEP and MACE exhibit excellent agreement with the DFT reference, with RMSE values of 364.4 meV Å⁻¹ and 109.3 meV Å⁻¹, respectively. In contrast, ReaxFF exhibits significantly larger deviations in force predictions, with a force RMSE more than one order of magnitude larger (7791.1 meV Å⁻¹, see Figure 1(d)), demonstrating considerably lower accuracy for the graphene oxide systems investigated here.

Although the accuracy of our NEP model is lower than that of MACE, which benefits from message-passing architectures and equivariant feature representations within its graph neural network framework [11, 28],

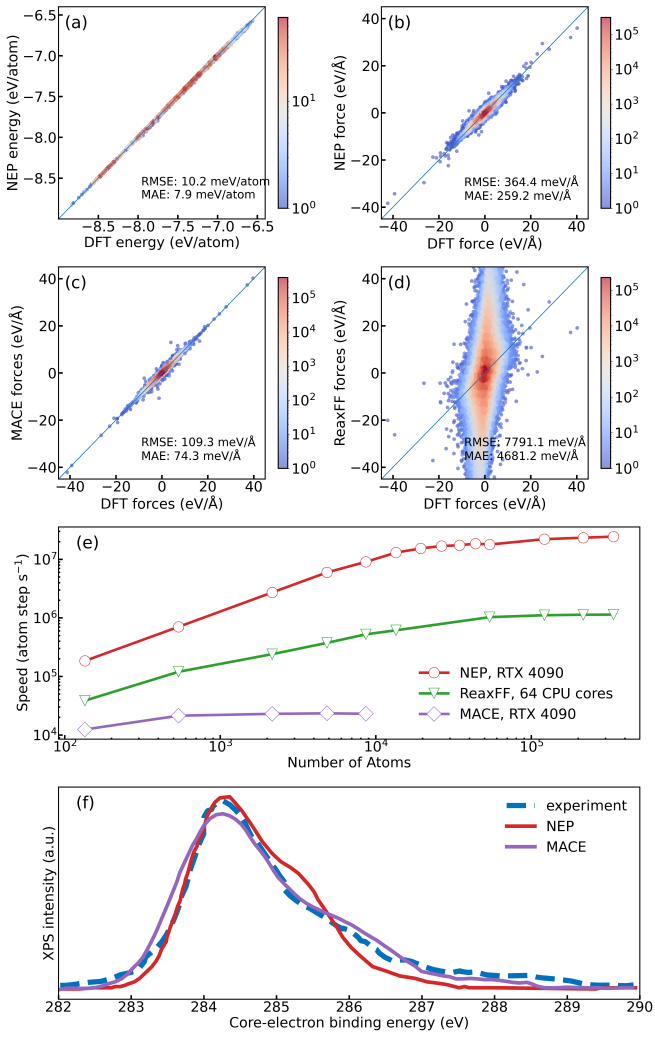


FIG. 1. Comparison of accuracy and computational speed for NEP, MACE, and ReaxFF models. (a) Correlation between DFT reference data and NEP predictions for total energy across the training set. (b-d) Comparison of predicted forces against DFT data for (b) NEP, (c) MACE and (d) ReaxFF across the train dataset. In panels (a)-(d), color intensity represents the local density of data points, and the corresponding RMSE and MAE values are provided. (e) Computational speed as a function of the number of atoms in the GO structure. NEP and MACE benchmarks were performed on a single RTX 4090 GPU (24 GB memory) using GPUMD (version 4.3) and ASE (version 3.23.0) packages, respectively; ReaxFF benchmarks were performed on 64 Xeon Platinum 8358P CPU cores (512 GB memory) using LAMMPS package (version 29 Aug 2024)). The MACE and ReaxFF models were obtained from Refs. [12] and [25], respectively. (f) XPS predictions for the rGO structure with an O/C ratio of 0.4 and OH/O ratio of 0.5. The NEP XPS profile was calculated for rGO annealed at 900 K and equilibrated at 300 K, using XPS prediction server provided by Ref. [26]. The NEP data were shifted horizontally to align with the experimental data from Ref. [27], while the MACE data were extracted from Ref. [12].

the primary reason for selecting NEP is its superior com-

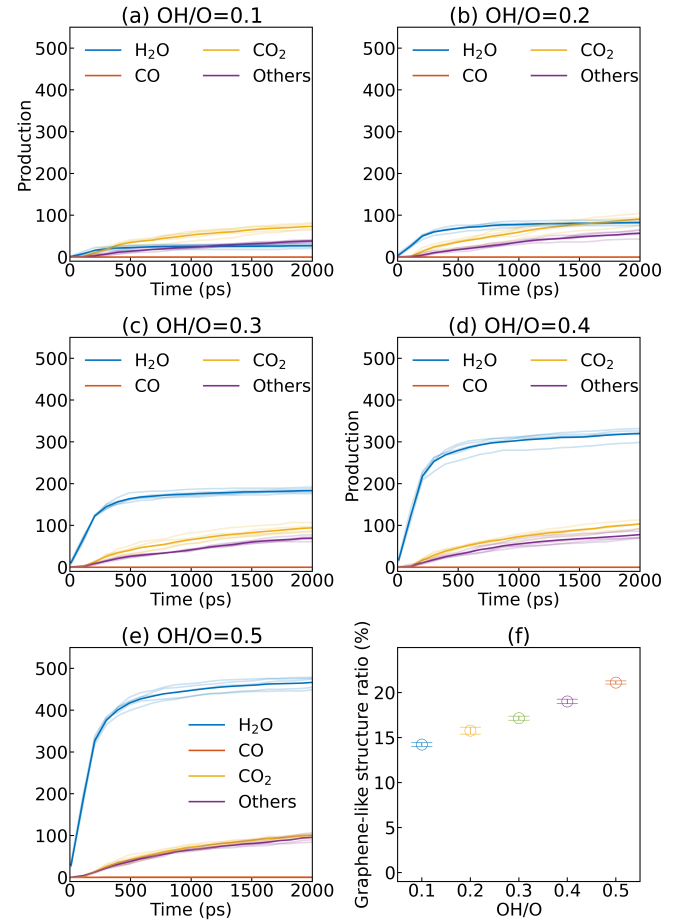


FIG. 2. Evolution of gaseous byproducts during thermal reduction of GO at 900 K with a fixed O/C ratio of 0.4. (a)-(e) Time-resolved production of H₂O, CO₂, CO, and other species during thermal reduction simulations, for initial OH/O ratios ranging from 0.1 to 0.5: (a) 0.1, (b) 0.2, (c) 0.3, (d) 0.4, and (e) 0.5. Each panel shows the average of five independent simulations (solid lines) with individual trajectories shown in translucence. (f) The ratio of graphene-like structures in the final configurations at 2000 ps as a function of initial OH/O ratio.

putational efficiency. This efficiency is crucial for thermal conductivity calculations, which require extensive sampling over long timescales and large system sizes.

To demonstrate this advantage, we performed a benchmark timing test using an initial GO structure generated with the parameter set $\mathbf{P} = [0.4, 0.5, 0]$ (containing 135 atoms). This unit cell was then replicated into supercells of increasing sizes. NVT-ensemble MD simulations were run for 2000 steps at 300 K using NEP, MACE, and ReaxFF. As shown in Figure 1 (e), the computational speed for all models initially increases with system size and reaches saturation for relatively larger systems.

Using a single RTX 4090 GPU, NEP implemented in the GPUMD package achieves a speed exceeding 1×10^7 atom step s⁻¹ for systems containing hundreds of thousands of atoms. In contrast, MACE imple-

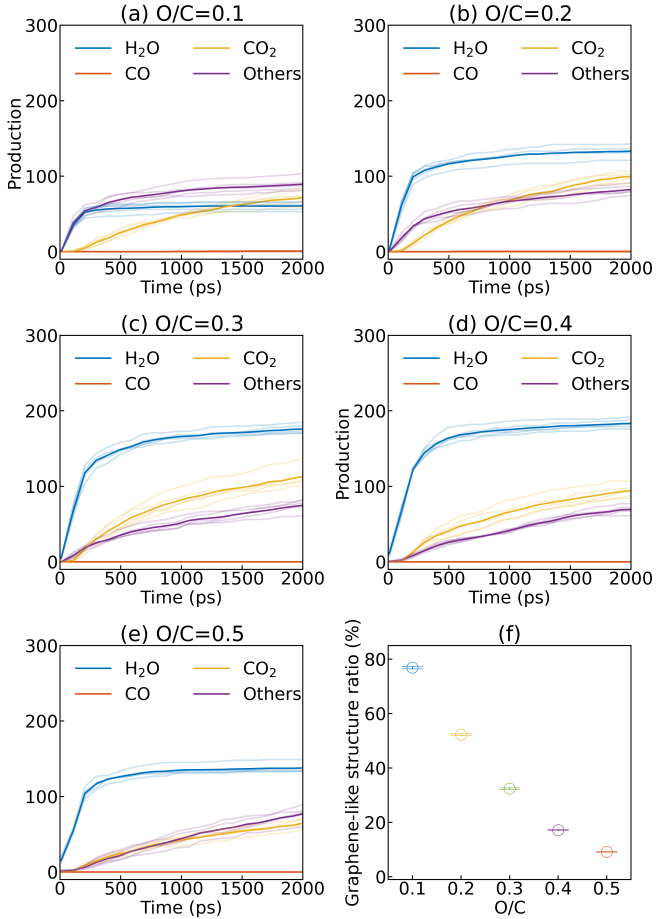


FIG. 3. Evolution of gaseous byproducts during thermal reduction of GO at 900 K with a fixed OH/O ratio of 0.3. (a)-(e) Time-resolved production of H₂O, CO₂, CO, and other species as during thermal reduction simulations, for initial O/C ratios ranging from 0.1 to 0.5: (a) 0.1, (b) 0.2, (c) 0.3, (d) 0.4, and (e) 0.5. Each panel shows the average of five independent simulations (solid lines) with individual trajectories shown in translucence. (f) The ratio of graphene-like structures in the final configurations at 2000 ps as a function of initial O/C ratio.

mented in the ASE package [29] is practical only for systems up to thousands of atoms, exhibiting a computational speed three orders of magnitude lower, near 1×10^4 atom step s⁻¹. Furthermore, compared with the empirical ReaxFF model implemented in the LAMMPS package [30] running on 64 CPU cores, our machine-learned NEP model demonstrates a computational speed that is more than one order of magnitude higher. These results justify the choice of the NEP model, as it offers the necessary balance of accuracy and efficiency required for the large-scale, long-timescale MD simulations in this study. We note that although the accuracy of NEP is relatively lower than that of MACE, NEP predicted a reasonable XPS profile for rGO after thermal reduction simulations (Figure 1(f)), which aligns well with experimental data [27] and MACE prediction [12], demon-

strating the reliability of our developed NEP model.

To elucidate the structural evolution during the thermal reduction of GO to rGO, we monitored the production of the primary gaseous byproducts through two complementary series of simulations: first by keeping the O/C ratio fixed while systematically varying the OH/O ratio (Figure 2), and second by keeping the OH/O ratio fixed while systematically varying the O/C ratio (Figure 3). To ensure statistical reliability, we performed five independent thermal reduction simulations for each set of OH/O and O/C ratios. We quantified the fraction of "graphene-like" atoms in the resulting rGO structure using polyhedral template matching (PTM) [31] as implemented in OVITO [32] applying a root mean square deviation (RMSD) cutoff of 0.15.

As shown in Figure 2 (a)-(e), where the O/C ratio is fixed at 0.4 and the OH/O ratio ranges from 0.1 to 0.5, the major desorption products are H₂O (blue line), CO₂ (yellow line), CO (pink line), and a small fraction of other species (purple line). We further observe that increasing the initial OH/O ratio leads to a substantial rise in the total yield of gaseous byproducts. Among these, H₂O production is most strongly influenced, exhibiting the sharpest increase with higher hydroxyl content. In contrast, while CO evolution was monitored throughout the simulations, its final yield remains negligible across all studied ratios. Figure 2(f) reports the structural quality of the final reduced frames. As the initial OH/O ratio increases, the recovery of the graphene lattice, evidenced by the fraction of PTM-identified hexagonal environments, exhibits a noticeable improvement. Specifically, it rises from $\sim 14\%$ at OH/O = 0.1 to $\sim 21\%$ at OH/O = 0.5, representing an approximate 50% relative increase. This structural restoration is attributed to the preferential desorption of oxygen as H₂O at higher hydroxyl concentrations, a non-destructive pathway that preserves the underlying carbon skeleton, whereas lower OH/O ratios favor carbon-consuming pathways, with CO₂ evolution acting as the dominant source of carbon loss, which generates lattice vacancies.

In a complementary analysis, we fixed the OH/O ratio at 0.3 while systematically varying the O/C ratio from 0.1 to 0.5 to investigate the influence of overall oxygen content on the thermal reduction process (see Figure 3). As illustrated in the gas evolution profiles (Figure 3(a)-(e)), unlike the OH/O variation, changes in the O/C ratio do not drive a continuous increase in H₂O evolution; instead, H₂O production saturates and even exhibits a moderate decrease at high O/C ratios (0.4–0.5). Crucially, while CO₂ production plateaus between O/C = 0.3 and 0.4, there is a marked rise in the evolution of 'other' gaseous byproducts for O/C=0.5 (see purple line in Figure 3(e)). This indicates that at the highest oxidation levels, carbon etching is increasingly driven by these alternative decomposition pathways alongside CO₂. Most notably, the PTM analysis (Figure 3(f)) reveals a drastic degradation in structural quality: the fraction of graphene-like carbon significantly drops from 77% at

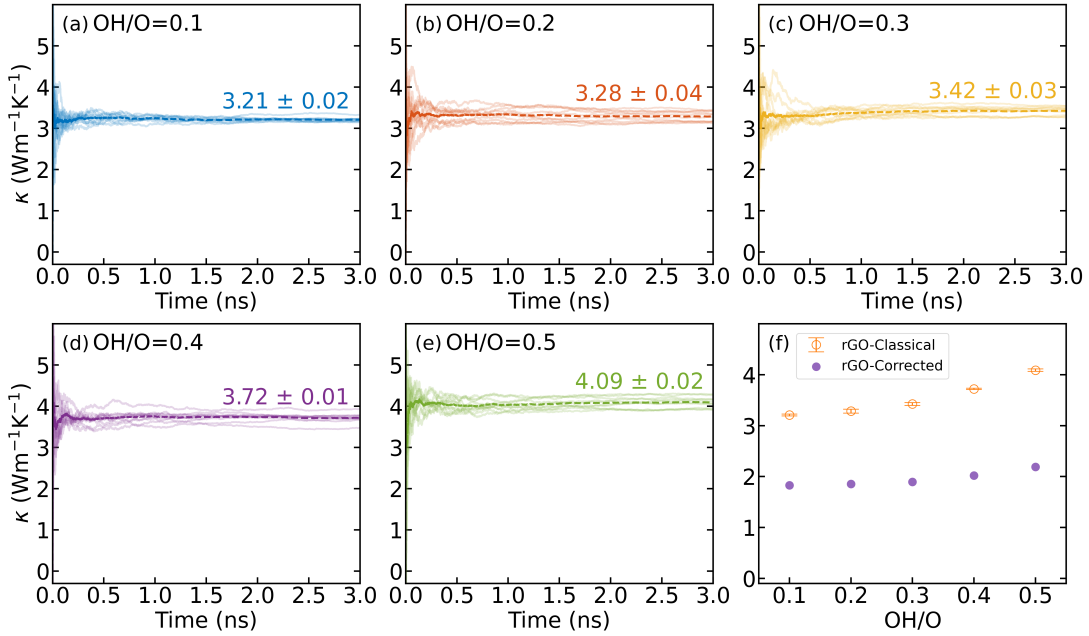


FIG. 4. Thermal conductivity of rGO structures obtained from HNEMD simulations with a fixed initial O/C ratio of 0.4 and varying initial OH/O ratios. (a–e) Running thermal conductivity for OH/O ratio of (a) 0.1, (b) 0.2, (c) 0.3, (d) 0.4, and (e) 0.5, respectively. In each panel, translucent lines represent ten independent trajectories, while the solid dashed line shows the ensemble mean. The annotated values represent the average thermal conductivity and corresponding standard error calculated at 3 ns. (f) Summary comparing the average classical (hollow circles with error bars) and quantum-corrected (solid dots) thermal conductivity as a function of the initio OH/O ratio.

O/C = 0.1 to just 9% at O/C = 0.5. This confirms that higher initial oxygen content activates aggressive carbon-consuming reaction channels, shifting from simple CO₂ evolution to complex fragmentation, severely hindering the restoration of the pristine graphitic network.

We computed the thermal conductivity of the resulting rGO structures using the HNEMD simulations based on Equation 2 (see Figure 4 and Figure 5). For each set of O/C and OH/O ratios, we performed ten independent simulations (two lateral directions for each of the five configurations from independent thermal reduction simulations) to ensure statistical robustness. As the running thermal conductivity stabilizes at 3 ns (Figure 4(a)–(e)) and Figure 3(a)–(e)); production values were calculated from this point, with error bars representing the standard error of the mean.

In Figure 4(f), for the series with a fixed initial O/C ratio of 0.4, we observe that increasing the initial OH/O ratio leads to a moderate enhancement in the classical thermal conductivity of the rGO structures. Specifically, the conductivity rises from 3.21 ± 0.02 W m⁻¹ K⁻¹ at OH/O = 0.1 to 4.09 ± 0.02 W m⁻¹ K⁻¹ at OH/O = 0.5, representing an $\sim 27\%$ increase. In sharp contrast, a substantial decrease in the classical thermal conductivity of the rGO structures was observed at a fixed OH/O ratio of 0.3 as the O/C ratio increased from 0.1 to 0.5. This results in an order-of-magnitude reduction, dropping from 25.73 ± 0.46 W m⁻¹ K⁻¹ at O/C = 0.1 to 2.16 ± 0.02 W m⁻¹ K⁻¹ at OH/O = 0.5.

We attribute the enhancement in thermal conductivity at higher OH/O and lower O/C ratios to two synergistic factors: structural restoration and mechanical stiffening. First, the substantial rise in the graphene-like carbon fraction (Figure 2(f) and Figure 3(f)) creates more continuous and interconnected transport pathways, effectively suppressing phonon scattering and damping. Second, this structural recovery at higher OH/O and lower O/C ratios increases the material's Young's modulus [33]; this stiffening is directly linked to higher phonon group velocities, which further accelerate heat propagation through the lattice. Notably, we find that the thermal conductivity of rGO is much more sensitive to O/C ratio than OH/O ratio, because low O/C ratios significantly suppress carbon-consuming gaseous byproducts (Figure 3(a)), thereby preserving the carbon skeleton and leading to a much stronger dependence of the graphene-like structure fraction on the initial oxygen content.

Given the strong structural disorder in rGO and this system has high vibrational frequencies, accurate thermal transport predictions require accounting for nuclear quantum effects. While path-integral techniques [34] capture these effects, it is currently incompatible with thermal conductivity calculations due to the nonlinearity of the heat current operator [35]. Therefore, we adopted a feasible quantum-correction method based on the harmonic approximation, which has been rigorously validated for disordered materials [36–38] and even liquid water [39, 40]. This is achieved by multiplying it by the

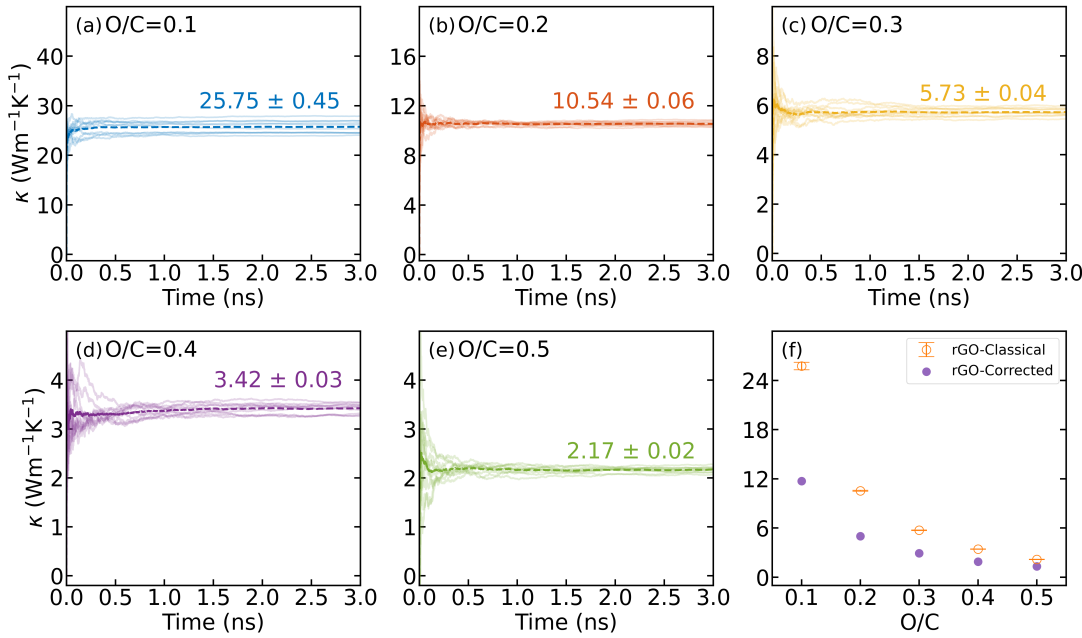


FIG. 5. Thermal conductivity of rGO structures obtained from HNEMD simulations with a fixed initial OH/O ratio of 0.3 and varying initial O/C ratios. (a–e) Running thermal conductivity for O/C ratio of (a) 0.1, (b) 0.2, (c) 0.3, (d) 0.4, and (e) 0.5, respectively. In each panel, translucent lines represent ten independent trajectories, while the solid dashed line shows the ensemble mean. The annotated values represent the average thermal conductivity and corresponding standard error calculated at 3 ns. (f) Summary comparing the average classical (hollow circles with error bars) and quantum-corrected (solid dots) thermal conductivity as a function of the initio O/C ratio.

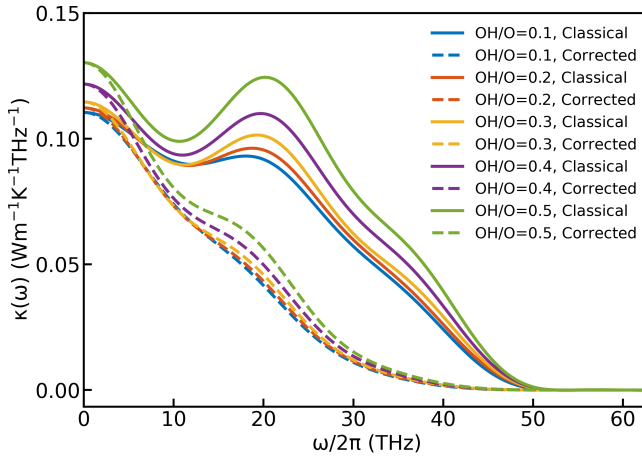


FIG. 6. Classical (solid lines) and quantum-corrected (dash lines) spectral thermal conductivity, $\kappa(\omega)$, as a function of phonon frequency for rGO structures with a fixed O/C ratio of 0.4 and varying OH/O ratios from 0.1 to 0.5. Each curve denotes the average of ten independent runs (two orthogonal in-plane directions across five separately generated structures) to ensure statistical robustness.

ratio between quantum and classical modal heat capacities [41–43]:

$$\kappa^q(\omega) = \kappa(\omega) \frac{x^2 e^x}{(e^x - 1)^2}, \quad (7)$$

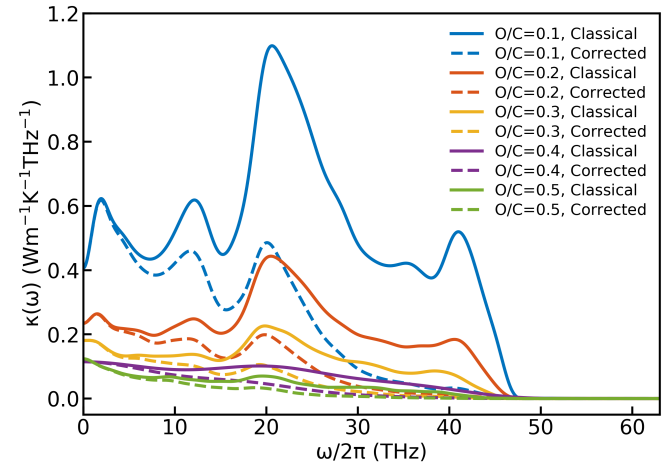


FIG. 7. Classical (solid lines) and quantum-corrected (dash lines) spectral thermal conductivity, $\kappa(\omega)$, as a function of phonon frequency for rGO structures with a fixed OH/O ratio of 0.3 and varying O/C ratios from 0.1 to 0.5. Each curve denotes the average of ten independent runs (two orthogonal in-plane directions across five separately generated structures) to ensure statistical robustness.

where $\kappa^q(\omega)$ and $\kappa(\omega)$ are classical and quantum-corrected spectral thermal conductivity, respectively, and $x = \hbar\omega/k_B T$, with \hbar the reduced Planck constant and k_B the Boltzmann constant. We emphasize that this

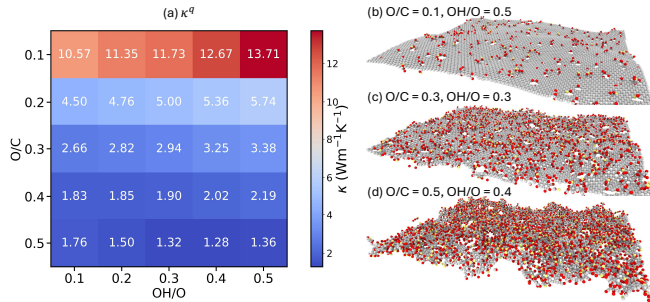


FIG. 8. (a) Computed quantum-corrected thermal conductivity (κ^q) of rGO structures across the full range of investigated compositional ratios. The heatmap displays the ensemble-averaged conductivity as a function of the initial O/C and OH/O ratios. For each grid point, the reported value represents the mean obtained from ten independent HNEMD simulations (comprising heat transport calculations along two orthogonal in-plane directions for five independent structural models generated from separate thermal reduction trajectories). (b-d) Three representative atomic snapshots for rGO showing the (b) highest κ^q (O/C = 0.1, OH/O = 0.5), (c) intermediate κ^q (O/C = 0.3, OH/O = 0.3), and (d) lowest κ^q (O/C = 0.5, OH/O = 0.4). Visualizations were created using OVITO package [32], with carbon, oxygen, and hydrogen atoms colored gray, red, and yellow, respectively.

quantum-correction approach is valid primarily in disordered systems, where vibrational modes exhibit short lifetimes and mean free paths. In such cases, the population effects on elastic scattering processes remain negligible, justifying the simple multiplicative heat-capacity correction.

To implement this correction, we decomposed the total thermal conductivity κ from HNEMD calculations performed at 300 K into its frequency-resolved spectral counterpart $\kappa(\omega)$ using Equation 6. Figure 6 and Figure 7 present both the classical and quantum-corrected spectral thermal conductivity curves for each investigated OH/O and O/C ratio. Upon integrating $\kappa^q(\omega)$ for all ratios of rGO at 300 K in Figure 7 and Figure 6, we present the quantum-corrected κ in Figure 4 (f) and Figure 5 (f) with solid circles. For the OH/O series (Figure 4), the $\kappa(\omega)$ profile exhibits remarkable similarity across all ratios, consistently featuring a single dominant peak at ~ 20 THz. This similarity persists after quantum correction, which simply scales down the high-frequency contributions. In contrast, varying the O/C ratio (Figure 5) significantly alters the spectral features. Unlike the uniform profiles observed in the OH/O series, the low O/C structures (0.1 and 0.2) display a complex multi-peak structure with distinct contributions at ~ 2 THz, ~ 12 THz, ~ 20 THz, and ~ 41 THz. However, as the O/C ratio increases, these features are progressively suppressed, resulting in a featureless profile at high oxidation levels. The quantum correction further dampens these high-frequency modes. Finally, compared with the classical κ , the quantum-corrected κ^q are reduced by

$\sim 45\%$ to $\sim 60\%$ across all structures.

TABLE I. Comparison of thermal conductivity κ ($\text{W m}^{-1} \text{K}^{-1}$) of monolayer 2D materials, including GO, rGO, graphene, qHP (quasi-hexagonal phase) and qTP (quasi-tetragonal phase) fullerene systems, phosphorene (P), MoS₂, and *h*-BN. For the rGO, GO, and graphene structures calculated in this work, the reported values for rGO and GO include quantum corrections. Predictions obtained via HNEMD, NEMD (nonequilibrium molecular dynamics), EMD (equilibrium molecular dynamics), and BTE (Boltzmann transport equation) methods as well as experimental measurements, are included for comparison.

Monolayer 2D materials	Method	κ
rGO (This work)	HNEMD	1.28– 13.71
rGO (3–5 nm thickness) [44]	Experiment	0.14– 2.87
rGO (1 nm thickness) [45]	Experiment	18(2)
GO (This work)	HNEMD	2.89 – 13.98
GO (O/C ≤ 0.04) [46]	NEMD	~40 – ~420
GO (O/C ≤ 0.2) [47]	NEMD	18–75
GO (0.05 ≤ O/C ≤ 0.2) [48]	NEMD	8.8–28.8
graphene (This work)	HNEMD	1391(43)
graphene [49]	Experiment	1689–1813
graphene [50]	HNEMD	1855(56)
graphene [51]	EMD	2900(100)
graphene [52]	HNEMD	2807.3
graphene [52]	EMD	3067.4
blue phosphorene [53]	HNEMD	128(3)
violet P [53]	HNEMD	2.36(0.05)
black P (zigzag) [53]	HNEMD	78.4(0.4)
black P (armchair) [53]	HNEMD	12.5(0.2)
MoS ₂ [54]	HNEMD	150.4 (6.2)
MoS ₂ [55]	Experiment	86, 100
qHP-x C ₂₄ [56]	HNEMD	233(5)
qHP-y C ₂₄ [56]	HNEMD	341(9)
qTP-C ₂₄ [56]	HNEMD	272(9)
qHP-x C ₆₀ [57]	HNEMD	102(3)
qHP-y C ₆₀ [57]	HNEMD	107(7)
<i>h</i> -BN [58]	HNEMD	544(10)
<i>h</i> -BN [59]	Experiment	751
α -graphyne [60]	BTE	21.11
biphenylene (armchair) [61]	BTE	166
biphenylene (zigzag) [61]	BTE	254
biphenylene (armchair) [52]	HNEMD	213.1
biphenylene (zigzag) [52]	HNEMD	203.5
biphenylene (armchair) [52]	EMD	232.3
biphenylene (zigzag) [52]	EMD	226.3

To provide a comprehensive overview, we computed the quantum-corrected thermal conductivity, κ^q , for the full range of initial O/C and OH/O ratios, as summarized in the heatmap in Figure 8. The results confirm that κ^q is predominantly governed by the O/C ratio, decreasing by an order of magnitude as the initial oxidation level increases from 0.1 to 0.5. In contrast, increasing the OH/O ratio consistently yields a moderate enhancement in thermal conductivity for O/C ratio below 0.5, reflecting the improved recovery of the graphene lattice discussed earlier. However, a notable exception is observed at the highest oxidation level (O/C = 0.5), where κ^q slightly

decreases with increasing OH/O ratio. This inversion suggests that at saturation coverage, the high density of hydroxyl groups may trigger aggressive decomposition pathways or defect clustering, likely analogous to oxidative etching [62], that outweighs the lattice-healing effects observed at lower oxidation levels (see Figure 8(b-d)). Consequently, we observe a maximum rGO thermal conductivity of $13.71 \text{ W m}^{-1} \text{ K}^{-1}$ (Figure 8(b); at O/C = 0.1, OH/O = 0.5), and a minimum of $1.28 \text{ W m}^{-1} \text{ K}^{-1}$ (Figure 8(d); at O/C = 0.5, OH/O = 0.4).

Finally, Table I benchmarks our calculated κ^q values against other monolayer 2D materials. The predicted thermal conductivity of rGO ($1.28 \text{ W m}^{-1} \text{ K}^{-1}$ to $13.71 \text{ W m}^{-1} \text{ K}^{-1}$) falls within the range of experimental measurements for samples with similar carbon ratios [44, 45], which is orders of magnitude lower than that of pristine graphene ($>1000 \text{ W m}^{-1} \text{ K}^{-1}$) and hexagonal boron nitride, but is comparable to violet phosphorene and black phosphorene, highlighting its potential for thermoelectric applications [63] where low thermal conductivity is advantageous.

Our simulations estimate that the thermal conductivity of rGO is comparable to or even lower than that of the initial GO models ($4.79 \text{ W m}^{-1} \text{ K}^{-1}$ to $30.00 \text{ W m}^{-1} \text{ K}^{-1}$, lowest at OH/O=O/C=0.5, highest at OH/O=O/C=0.1), a trend that contrasts with previous experimental measurements where conductivity typically increases after reduction [4]. We attribute this discrepancy to two factors. First, our initial GO models were constructed on ideal graphene lattices without atomic vacancies; consequently, the thermal reduction process, which drives carbon loss and vacancy formation, effectively degrades the phonon transport relative to the pristine starting state. Second, experimental GO and rGO are typically multi-layer systems, where high-temperature annealing facilitates defect healing across layers [64], a recovery mechanism not present in our monolayer simulations. We leave the investigation of these effects for future work; our present study therefore serves as a foundation for further understanding thermal transport in multi-layer and bulk rGO and GO systems.

IV. SUMMARY AND CONCLUSIONS

In summary, we have established a computationally efficient and predictive atomistic framework to investigate the complex interplay between chemical reduction and thermal transport in GO. By developing a neuroevolution potential (NEP-GO) trained on DFT data, we achieved a computational speedup of several orders of magnitude compared to MACE and ReaxFF models while maintaining a reasonable accuracy. This capability enabled large-scale, long-timescale MD simulations of thermal reduction and heat transport that were previously computationally prohibitive.

Our simulations reveal that the thermal conductivity of rGO is not solely governed by the degree of oxidation

alone but is critically dependent on the specific chemical composition of the initial state. We identified two distinct structural evolution pathways: (i) generally, increasing the initial OH/O ratio promotes non-destructive water desorption, leading to substantial lattice recovery and enhanced thermal transport, though this trend inverts at the highest oxidation level (O/C = 0.5) where hydroxyl saturation triggers aggressive lattice disruption rather than healing; and (ii) increasing the initial O/C ratio activates aggressive carbon-etching pathways via CO and CO₂ evolution, resulting in severe defect formation and suppressed thermal conductivity. Furthermore, by decomposing the thermal conductivity into its spectral components and applying quantum-statistical corrections, we demonstrated that nuclear quantum effects significantly suppress high-frequency vibrational modes in these disordered systems, reducing the predicted thermal conductivity by approximately 50% compared to classical predictions.

Quantitatively, the quantum-corrected thermal conductivity of monolayer rGO spans a range of $1.28 \text{ W m}^{-1} \text{ K}^{-1}$ to $13.71 \text{ W m}^{-1} \text{ K}^{-1}$. While these values are orders of magnitude lower than pristine graphene, they render rGO a promising candidate for thermoelectric applications where low lattice thermal conductivity is desirable. By demonstrating how the specific ratios of oxygen functional groups can be tuned to design target thermal conductivities, we pave the way for future investigations that extend these principles to topological structures and multi-layer bulk systems, ultimately enabling precise defect-engineering strategies for advanced thermal management.

ACKNOWLEDGMENTS

This work is supported by the National Science and Technology Advanced Materials Major Program of China (No. 2024ZD0606900). ZF is supported by the Science Foundation from Education Department of Liaoning Province (No. LJ232510167001). Jinglei Yang and the HKUST personnel are supported by the Project of Hetao Shenzhen-Hong Kong Science and Technology Innovation Cooperation Zone (HZQB-KCZYB-2020083) and the Innovation and Technology Commission of Hong Kong (ITC-CNERC14SC01).

Data availability:

Complete input and output files for the NEP-GO model are freely available at <https://gitlab.com/brucefan1983/nep-data>. All rGO structures obtained from thermal reduction simulations are available in extended xyz format on Zenodo at <https://doi.org/10.5281/zenodo.18027655>.

Declaration of competing interest:

The authors declare that they have no competing in-

terests.

-
- [1] D. R. Dreyer, S. Park, C. W. Bielawski, and R. S. Ruoff, The chemistry of graphene oxide, *Chem. Soc. Rev.* **39**, 228 (2010).
- [2] C. K. Chua and M. Pumera, Chemical reduction of graphene oxide: a synthetic chemistry viewpoint, *Chem. Soc. Rev.* **43**, 291 (2014).
- [3] Y. Y. Khine, X. Wen, X. Jin, T. Foller, and R. Joshi, Functional groups in graphene oxide, *Phys. Chem. Chem. Phys.* **24**, 26337 (2022).
- [4] J. D. Renteria, S. Ramirez, H. Malekpour, B. Alonso, A. Centeno, A. Zurutuza, A. I. Cocemasov, D. L. Nika, and A. A. Balandin, Strongly anisotropic thermal conductivity of free-standing reduced graphene oxide films annealed at high temperature, *Adv. Funct. Mater.* **25**, 4664 (2015).
- [5] S. Jin, Q. Gao, X. Zeng, R. Zhang, K. Liu, X. Shao, and M. Jin, Effects of reduction methods on the structure and thermal conductivity of free-standing reduced graphene oxide films, *Diam. Relat. Mater.* **58**, 54 (2015).
- [6] A. C. Van Duin, S. Dasgupta, F. Lorant, and W. A. Goddard, ReaxFF: a reactive force field for hydrocarbons, *The Journal of Physical Chemistry A* **105**, 9396 (2001).
- [7] J.-H. Zou, Z.-Q. Ye, and B.-Y. Cao, Phonon thermal properties of graphene from molecular dynamics using different potentials, *J. Chem. Phys.* **145**, 134705 (2016).
- [8] C. Diao, Y. Dong, and J. Lin, Reactive force field simulation on thermal conductivities of carbon nanotubes and graphene, *Int. J. Heat Mass Transfer* **112**, 903 (2017).
- [9] J. Behler and M. Parrinello, Generalized Neural-Network Representation of High-Dimensional Potential-Energy Surfaces, *Phys. Rev. Lett.* **98**, 146401 (2007).
- [10] A. P. Bartók, M. C. Payne, R. Kondor, and G. Csányi, Gaussian approximation potentials: The accuracy of quantum mechanics, without the electrons, *Phys. Rev. Lett.* **104**, 136403 (2010).
- [11] I. Batatia, D. P. Kovacs, G. Simm, C. Ortner, and G. Csányi, Mace: Higher order equivariant message passing neural networks for fast and accurate force fields, *Advances in neural information processing systems* **35**, 11423 (2022).
- [12] Z. El-Machachi, D. Frantzov, A. Nijamudheen, T. Zarrouk, M. A. Caro, and V. L. Deringer, Accelerated first-principles exploration of structure and reactivity in graphene oxide, *Angewandte Chemie International Edition* **63**, e202410088 (2024).
- [13] H. Dong, Y. Shi, P. Ying, K. Xu, T. Liang, Y. Wang, Z. Zeng, X. Wu, W. Zhou, S. Xiong, S. Chen, and Z. Fan, Molecular dynamics simulations of heat transport using machine-learned potentials: A mini-review and tutorial on GPUMD with neuroevolution potentials, *Journal of Applied Physics* **135**, 161101 (2024).
- [14] Z. Fan, Z. Zeng, C. Zhang, Y. Wang, K. Song, H. Dong, Y. Chen, and T. Ala-Nissila, Neuroevolution machine learning potentials: Combining high accuracy and low cost in atomistic simulations and application to heat transport, *Phys. Rev. B* **104**, 104309 (2021).
- [15] Z. Fan, Y. Wang, P. Ying, K. Song, J. Wang, Y. Wang, Z. Zeng, K. Xu, E. Lindgren, J. M. Rahm, A. J. Gabourie, J. Liu, H. Dong, J. Wu, Y. Chen, Z. Zhong, J. Sun, P. Erhart, Y. Su, and T. Ala-Nissila, GPUMD: A package for constructing accurate machine-learned potentials and performing highly efficient atomistic simulations, *The Journal of Chemical Physics* **157**, 114801 (2022).
- [16] K. Song, R. Zhao, J. Liu, Y. Wang, E. Lindgren, Y. Wang, S. Chen, K. Xu, T. Liang, P. Ying, N. Xu, Z. Zhao, J. Shi, J. Wang, S. Lyu, Z. Zeng, S. Liang, H. Dong, L. Sun, Y. Chen, Z. Zhang, W. Guo, P. Qian, J. Sun, P. Erhart, T. Ala-Nissila, Y. Su, and Z. Fan, General-purpose machine-learned potential for 16 elemental metals and their alloys, *Nature Communications* **15**, 10208 (2024).
- [17] P. Ying, C. Qian, R. Zhao, Y. Wang, K. Xu, F. Ding, S. Chen, and Z. Fan, Advances in modeling complex materials: The rise of neuroevolution potentials, *Chemical Physics Reviews* **6**, 011310 (2025).
- [18] K. Xu, H. Bu, S. Pan, E. Lindgren, Y. Wu, Y. Wang, J. Liu, K. Song, B. Xu, Y. Li, T. Hainer, L. Svensson, J. Wiktor, R. Zhao, H. Huang, C. Qian, S. Zhang, Z. Zeng, B. Zhang, B. Tang, Y. Xiao, Z. Yan, J. Shi, Z. Liang, J. Wang, T. Liang, S. Cao, Y. Wang, P. Ying, N. Xu, C. Chen, Y. Zhang, Z. Chen, X. Wu, W. Jiang, E. Berger, Y. Li, S. Chen, A. J. Gabourie, H. Dong, S. Xiong, N. Wei, Y. Chen, J. Xu, F. Ding, Z. Sun, T. Ala-Nissila, A. Harju, J. Zheng, P. Guan, P. Erhart, J. Sun, W. Ouyang, Y. Su, and Z. Fan, Gpumd 4.0: A high-performance molecular dynamics package for versatile materials simulations with machine-learned potentials, *Materials Genome Engineering Advances* **3**, e70028 (2025).
- [19] T. Schaul, T. Glasmachers, and J. Schmidhuber, High dimensions and heavy tails for natural evolution strategies (Association for Computing Machinery, New York, NY, USA, 2011).
- [20] G. Bussi and M. Parrinello, Accurate sampling using langevin dynamics, *Phys. Rev. E* **75**, 056707 (2007).
- [21] Z. Fan, H. Dong, A. Harju, and T. Ala-Nissila, Homogeneous nonequilibrium molecular dynamics method for heat transport and spectral decomposition with many-body potentials, *Phys. Rev. B* **99**, 064308 (2019).
- [22] G. Bussi, D. Donadio, and M. Parrinello, Canonical sampling through velocity rescaling, *The Journal of Chemical Physics* **126**, 014101 (2007).
- [23] D. J. Evans, Homogeneous NEMD algorithm for thermal conductivity—Application of non-canonical linear response theory, *Physics Letters A* **91**, 457 (1982).
- [24] Z. Fan, L. F. C. Pereira, H.-Q. Wang, J.-C. Zheng, D. Donadio, and A. Harju, Force and heat current formulas for many-body potentials in molecular dynamics simulations with applications to thermal conductivity calculations, *Phys. Rev. B* **92**, 094301 (2015).
- [25] M. Kowalik, C. Ashraf, B. Damirchi, D. Akbarian, S. Rajabpour, and A. C. Van Duin, Atomistic scale analysis of the carbonization process for C/H/O/N-based polymers with the ReaxFF reactive force field, *The Journal of Physical Chemistry B* **123**, 5357 (2019).

- [26] D. Golze, M. Hirvensalo, P. Hernández-León, A. Aarva, J. Etula, T. Susi, P. Rinke, T. Laurila, and M. A. Caro, Accurate computational prediction of core-electron binding energies in carbon-based materials: A machine-learning model combining density-functional theory and gw, *Chemistry of Materials* **34**, 6240 (2022).
- [27] C. Valentini, V. Montes-García, P. A. Livio, T. Chudziak, J. Raya, A. Ciesielski, and P. Samori, Tuning the electrical properties of graphene oxide through low-temperature thermal annealing, *Nanoscale* **15**, 5743 (2023).
- [28] D. P. Kovács, I. Batatia, E. S. Arany, and G. Csányi, Evaluation of the MACE force field architecture: From medicinal chemistry to materials science, *The Journal of Chemical Physics* **159**, 044118 (2023).
- [29] A. Hjorth Larsen, J. Jørgen Mortensen, J. Blomqvist, I. E. Castelli, R. Christensen, M. Dułak, J. Friis, M. N. Groves, B. Hammer, C. Hargus, E. D. Hermes, P. C. Jennings, P. Bjerre Jensen, J. Kermode, J. R. Kitchin, E. Leonhard Kolsbjergrg, J. Kubal, K. Kaasbjerg, S. Lysgaard, J. Bergmann Maronsson, T. Maxson, T. Olsen, L. Pastewka, A. Peterson, C. Rostgaard, J. Schiøtz, O. Schütt, M. Strange, K. S. Thygesen, T. Vegge, L. Vilhelmsen, M. Walter, Z. Zeng, and K. W. Jacobsen, The atomic simulation environment—a python library for working with atoms, *Journal of Physics: Condensed Matter* **29**, 273002 (2017).
- [30] A. P. Thompson, H. M. Aktulga, R. Berger, D. S. Bolintineanu, W. M. Brown, P. S. Crozier, P. J. in 't Veld, A. Kohlmeyer, S. G. Moore, T. D. Nguyen, R. Shan, M. J. Stevens, J. Tranchida, C. Trott, and S. J. Plimpton, LAMMPS - a flexible simulation tool for particle-based materials modeling at the atomic, meso, and continuum scales, *Comp. Phys. Comm.* **271**, 108171 (2022).
- [31] P. M. Larsen, S. Schmidt, and J. Schiøtz, Robust structural identification via polyhedral template matching, *Modelling and Simulation in Materials Science and Engineering* **24**, 055007 (2016).
- [32] A. Stukowski, Visualization and analysis of atomistic simulation data with OVITO—the Open Visualization Tool, *Modelling and simulation in materials science and engineering* **18**, 015012 (2009).
- [33] Z. El-Machachi, B. Cheng, and V. L. Deringer, Mechanical properties of graphene oxide from machine-learning-driven simulations, *Chemical Communications* **61**, 11405 (2025).
- [34] P. Ying, W. Zhou, L. Svensson, E. Berger, E. Fransson, F. Eriksson, K. Xu, T. Liang, J. Xu, B. Song, *et al.*, Highly efficient path-integral molecular dynamics simulations with GPUMD using neuroevolution potentials: Case studies on thermal properties of materials, *The Journal of Chemical Physics* **162**, 064109 (2025).
- [35] Z. Zeng, Z. Fan, M. Simoncelli, C. Chen, T. Liang, Y. Chen, G. Thornton, and B. Cheng, Lattice distortion leads to glassy thermal transport in crystalline $\text{Cs}_3\text{Bi}_2\text{I}_6\text{Cl}_3$, *Proceedings of the National Academy of Sciences* **122**, e2415664122 (2025).
- [36] Y. Wang, Z. Fan, P. Qian, M. A. Caro, and T. Ala-Nissila, Quantum-corrected thickness-dependent thermal conductivity in amorphous silicon predicted by machine learning molecular dynamics simulations, *Physical Review B* **107**, 054303 (2023).
- [37] T. Liang, P. Ying, K. Xu, Z. Ye, C. Ling, Z. Fan, and J. Xu, Mechanisms of temperature-dependent thermal transport in amorphous silica from machine-learning molecular dynamics, *Phys. Rev. B* **108**, 184203 (2023).
- [38] Y. Wang, Z. Fan, P. Qian, M. A. Caro, and T. Ala-Nissila, Density dependence of thermal conductivity in nanoporous and amorphous carbon with machine-learned molecular dynamics, *Phys. Rev. B* **111**, 094205 (2025).
- [39] K. Xu, Y. Hao, T. Liang, P. Ying, J. Xu, J. Wu, and Z. Fan, Accurate prediction of heat conductivity of water by a neuroevolution potential, *The Journal of Chemical Physics* **158** (2023).
- [40] K. Xu, T. Liang, N. Xu, P. Ying, S. Chen, N. Wei, J. Xu, and Z. Fan, NEP-MB-pol: A unified machine-learned framework for fast and accurate prediction of water's thermodynamic and transport properties, *npj Computational Materials* **11**, 279 (2025).
- [41] Z. Fan, P. Hirvonen, L. F. C. Pereira, M. M. Ervasti, K. R. Elder, D. Donadio, A. Harju, and T. Ala-Nissila, Bimodal Grain-Size Scaling of Thermal Transport in Polycrystalline Graphene from Large-Scale Molecular Dynamics Simulations, *Nano Letters* **17**, 5919 (2017).
- [42] K. Sääskilahti, J. Oksanen, J. Tulkki, A. J. H. McGaughey, and S. Volz, Vibrational mean free paths and thermal conductivity of amorphous silicon from non-equilibrium molecular dynamics simulations, *AIP Advances* **6**, 121904 (2016).
- [43] W. Lv and A. Henry, Direct calculation of modal contributions to thermal conductivity via green-kubo modal analysis, *New Journal of Physics* **18**, 013028 (2016).
- [44] T. Schwamb, B. R. Burg, N. C. Schirmer, and D. Poulikakos, An electrical method for the measurement of the thermal and electrical conductivity of reduced graphene oxide nanostructures, *Nanotechnology* **20**, 405704 (2009).
- [45] N. K. Mahanta and A. R. Abramson, Thermal conductivity of graphene and graphene oxide nanoplatelets, in *13th intersociety conference on thermal and thermomechanical phenomena in electronic systems* (IEEE, 2012) pp. 1–6.
- [46] H. Zhang, A. F. Fonseca, and K. Cho, Tailoring thermal transport property of graphene through oxygen functionalization, *The Journal of Physical Chemistry C* **118**, 1436 (2014).
- [47] S. Lin and M. J. Buehler, Thermal transport in monolayer graphene oxide: Atomistic insights into phonon engineering through surface chemistry, *Carbon* **77**, 351 (2014).
- [48] X. Mu, X. Wu, T. Zhang, D. B. Go, and T. Luo, Thermal transport in graphene oxide – from ballistic extreme to amorphous limit, *Scientific Reports* **4**, 3909 (2014).
- [49] X. Xu, L. F. C. Pereira, Y. Wang, J. Wu, K. Zhang, X. Zhao, S. Bae, C. Tinh Bui, R. Xie, J. T. L. Thong, B. H. Hong, K. P. Loh, D. Donadio, B. Li, and B. Özyilmaz, Length-dependent thermal conductivity in suspended single-layer graphene, *Nature Communications* **5**, 3689 (2014).
- [50] X. Wu, W. Zhou, H. Dong, P. Ying, Y. Wang, B. Song, Z. Fan, and S. Xiong, Correcting force error-induced underestimation of lattice thermal conductivity in machine learning molecular dynamics, *The Journal of Chemical Physics* **161**, 014103 (2024).
- [51] Z. Fan, L. F. C. Pereira, P. Hirvonen, M. M. Ervasti, K. R. Elder, D. Donadio, T. Ala-Nissila, and A. Harju, Thermal conductivity decomposition in two-dimensional materials: Application to graphene, *Phys. Rev. B* **95**,

- 144309 (2017).
- [52] P. Ying, T. Liang, Y. Du, J. Zhang, X. Zeng, and Z. Zhong, Thermal transport in planar sp₂-hybridized carbon allotropes: A comparative study of biphenylene network, pentaheptite and graphene, *International Journal of Heat and Mass Transfer* **183**, 122060 (2022).
- [53] P. Ying, T. Liang, K. Xu, J. Xu, Z. Fan, T. Ala-Nissila, and Z. Zhong, Variable thermal transport in black, blue, and violet phosphorene from extensive atomistic simulations with a neuroevolution potential, *International Journal of Heat and Mass Transfer* **202**, 123681 (2023).
- [54] W. Jiang, H. Bu, T. Liang, P. Ying, Z. Fan, J. Xu, and W. Ouyang, Accurate modeling of interfacial thermal transport in van der waals heterostructures via hybrid machine learning and registry-dependent potentials (2025), arXiv:2505.00376 [physics.comp-ph].
- [55] X. Yang, X. Zheng, Q. Liu, T. Zhang, Y. Bai, Z. Yang, H. Chen, and M. Liu, Experimental study on thermal conductivity and rectification in suspended monolayer mos₂, *ACS Applied Materials & Interfaces* **12**, 28306 (2020).
- [56] Q. Li, H. Dong, P. Ying, and Z. Fan, Anisotropic and isotropic elasticity and thermal transport in monolayer c₂₄ networks from machine-learning molecular dynamics (2025), arXiv:2512.00362 [cond-mat.mtrl-sci].
- [57] H. Dong, C. Cao, P. Ying, Z. Fan, P. Qian, and Y. Su, Anisotropic and high thermal conductivity in monolayer quasi-hexagonal fullerene: A comparative study against bulk phase fullerene, *International Journal of Heat and Mass Transfer* **206**, 123943 (2023).
- [58] Z. Tan, S. Wang, Y. Liu, Y. Xiao, X. Zhou, S. Zhou, X. Xiu, and H. Dong, Coherent and incoherent phonon transport in graphene/h-bn superlattice: A machine learning potential, *Physica E: Low-dimensional Systems and Nanostructures* **172**, 116259 (2025).
- [59] Q. Cai, D. Scullion, W. Gan, A. Falin, S. Zhang, K. Watanabe, T. Taniguchi, Y. Chen, E. J. G. Santos, and L. H. Li, High thermal conductivity of high-quality monolayer boron nitride and its thermal expansion, *Science Advances* **5**, eaav0129 (2019).
- [60] X. Yang, Z. Dai, Y. Zhao, and S. Meng, Phonon thermal transport in a class of graphene allotropes from first principles, *Phys. Chem. Chem. Phys.* **20**, 15980 (2018).
- [61] H. P. Veeravenkata and A. Jain, Density functional theory driven phononic thermal conductivity prediction of biphenylene: A comparison with graphene, *Carbon* **183**, 893 (2021).
- [62] L. Liu, S. Ryu, M. R. Tomaszik, E. Stolyarova, N. Jung, M. S. Hybertsen, M. L. Steigerwald, L. E. Brus, and G. W. Flynn, Graphene oxidation: thickness-dependent etching and strong chemical doping, *Nano letters* **8**, 1965 (2008).
- [63] T. Li, A. D. Pickel, Y. Yao, Y. Chen, Y. Zeng, S. D. Lacey, Y. Li, Y. Wang, J. Dai, Y. Wang, *et al.*, Thermoelectric properties and performance of flexible reduced graphene oxide films up to 3,000 K, *Nature Energy* **3**, 148 (2018).
- [64] P. Ying, X. Gao, A. Natan, M. Urbakh, and O. Hod, Chemifriction and Superlubricity: Friends or Foes?, *The Journal of Physical Chemistry Letters* **16**, 2934 (2025).